JGR Space Physics

RESEARCH ARTICLE
10.1029/2021JA030075

Characteristics of the Effective Scale Height in the Topside Ionosphere Extracted From Swarm A and Digisonde Observations: Preliminary Results

A. Belehaki[1], I. Tsagouri[1], and E. Paouris[1]

[1]Institute of Astronomy, Astrophysics, Space Applications and Remote Sensing, National Observatory of Athens, Metaxa and Vas Pavlou, Greece

Key Points:

- A clear diurnal pattern is identified in the topside effective scale height with peak values in the early morning and evening sectors
- At night, the topside effective scale height tends to increase with altitude, while in the daytime its altitudinal dependence is complex
- Evidence for connection between spread F irregularities and high variability in the topside effective scale height is reported

Correspondence to:

A. Belehaki,
belehaki@noa.gr

Citation:

Belehaki, A., Tsagouri, I., & Paouris, E. (2022). Characteristics of the effective scale height in the topside ionosphere extracted from Swarm A and Digisonde observations: Preliminary results. *Journal of Geophysical Research: Space Physics*, *127*, e2021JA030075. https://doi.org/10.1029/2021JA030075

Received 24 OCT 2021
Accepted 23 JAN 2022

Author Contributions:

Conceptualization: A. Belehaki
Data curation: A. Belehaki
Formal analysis: A. Belehaki
Funding acquisition: A. Belehaki
Investigation: A. Belehaki
Methodology: A. Belehaki, I. Tsagouri
Project Administration: A. Belehaki
Software: A. Belehaki, E. Paouris
Supervision: A. Belehaki
Validation: A. Belehaki, I. Tsagouri
Visualization: A. Belehaki, E. Paouris
Writing – original draft: A. Belehaki
Writing – review & editing: A. Belehaki, I. Tsagouri

Abstract The ionospheric scale height is a key parameter that defines the shape of the electron density profile. Given that its direct calculation requires knowledge of the physical and chemical state of the plasma, the concept of the effective scale height was proposed to facilitate its application. It is defined as the scale height that fits the electron density profiles with the α-Chapman function. Its main characteristics, including the diurnal and altitudinal variation are still under investigation. This paper focuses on the specification of its key characteristics at middle latitudes based on coincident Digisonde and Swarm A satellite data. Based on the assumption that the topside electron density profile is approximated with the α-Chapman model of variable scale height, the effective scale height at the Swarm A altitude is calculated and compared with the effective scale height at *hmF*2. A general conclusion is that the topside effective scale height at ~450 km exhibits a diurnal variation with highest values in the early morning and evening sectors, while at *hmF*2 it gets its maximum values at noon. At night, the effective scale height tends to increase with altitude, however in the daytime, its behavior is more complex. On a local scale, evidence for connection between spread F irregularities and high variability in the topside effective scale height is reported. These preliminary results indicate the potential to further exploit Swarm and Digisonde data for the development of a model for the effective scale height, able to support realistic electron density reconstruction models.

1. Introduction

The plasma scale height Hp, is a critical ionospheric characteristic that defines the shape of the electron density profile (Belehaki et al., 2006; L. Liu et al., 2007; Stankov et al., 2003). The plasma scale height is connected, by its definition, with the ionospheric dynamics, plasma thermal structure and compositions (Luan et al., 2006; Stankov & Jakowski, 2006; Webb et al., 2006), as it is defined as $H_p = k_b T_p / m_i g$, where k_b is the Boltzmann constant, g is the acceleration due to gravity, m_i is the ion mass, and T_p is the plasma temperature, that includes both ions and electrons. Given that the calculation of the H_p requires knowledge of the physical state of the plasma temperature, chemical state, and mean ion mass for the whole profile, its application for operational purposes is difficult. This is why, a more direct and practical approach was developed based on the concept of the effective scale height proposed to be used for the reconstruction of a reliable picture for the electron density (Ne) profile Ne(h) including its topside part. The effective scale height is defined as the scale height in fitting the Ne profiles with the α-Chapman function. Reinisch and Huang (2001) introduced a technique to extrapolate the topside ionosphere based on the information from ground-based ionograms. They approximated Ne(h) around and above the F2 layer peak (*hmF*2) by the α-Chapman function with an effective scale height (Hm) determined at *hmF*2. The ionogram-derived Hm is a kind of measure of the slope of the Digisonde-derived electron density profiles in the topside ionosphere. This technique assumes that the effective scale height in the topside remains constant and equal to the effective scale height at the *hmF*2 altitude. However, the ionospheric total electron content (ITEC) calculated as the integral of the electron density with altitude resulted with this method, underestimates the plasmaspheric contribution, as shown by Belehaki et al. (2003).

Later on, the growing bulk of topside measurements suggested the need to allow for a more general function of the scale height in respect to height (dos Santos Prol et al., 2019; Hernández-Pajares, Garcia-Fernández, et al., 2017; Nsumei et al., 2012; Olivares-Pulido et al., 2016; Wang et al., 2015; Wu et al., 2020). The majority of these studies rely on statistical analysis and provide the statistical pattern of the effective scale height variability.

L. Liu et al. (2007) analyzed the electron density profiles from the Arecibo Incoherent Scatter Radar (ISR) to examine the daily variation of the effective scale height in the lower topside ionosphere. The median ISR Ne profiles obtained within every 30-min interval every day are used for this analysis, resulted to more than 16,000 mean profiles. Every median Ne profile within 160–600 km is fitted using an α-Chapman function but with a scale height Hm independent of altitude. Thus, the peak electron density (N_mF2), its height ($hmF2$), and Hm are determined from the least squares fitting procedure. The median values of Hm have solar activity dependency. There are two peaks in the diurnal variations of Hm, one in the early morning and another one located in the afternoon to the evening sector. After the morning peak, Hm descend. Next, they approach a minimum at 6–8 Local Time (LT) and rise again, reaching maximum in the evening. Later they tend to decrease again till midnight. In summer, the first peak shifts to later time. Moreover, the sunrise descent is marked in spring and autumn and most intensely in winter, while the trend during this time is opposite in summer. In the morning, the values of Hm are highest in summer and lowest in winter; while at rest time, the seasonal variation is less distinct.

Olivares-Pulido et al. (2016) presented results based on occultation data from the Constellation Observing System for Meteorology, Ionosphere, and Climate/FORMO SATellite-3 (COSMIC/FORMOSAT-3) Global Positioning System (GPS), inverted by means of the Improved Abel transform inversion technique. They demonstrated that the scale height presents a linear trend above the F2 layer peak height, which is in good agreement with the expected linear temperature dependence. Results based on data from the northern hemisphere from four individual days suggest that scale height at the maximum of the peak, show significant dependency on LT and latitude. The scale height reaches the biggest values in winter, which in general, ranges from 35 to 50 km. In spring it remains constrained between 30 and 40 km. The minimum is reached in the summer when it is usually smaller than 40 km and even smaller than 30 km at dawn.

Park et al. (2015) estimated the α-Chapman scale height of the plasma density Hm in the topside ionospheric F-region around the Korean Peninsula using the Swarm constellation and ionosondes in Korea. The scale height has been calculated from plasma density data of Swarm Langmuir Probe (LP) and $foF2/hmF2$ data of two Korean ionosondes (Icheon and Jeju) for the period from 09 December 2013 to 30 June 2015. From the statistical distribution of the scale height with respect to LT and season, it is concluded that Hm above Korean Peninsula exhibits complex seasonal and LT dependence. The season-LT dependence agrees with that of Tulasi Ram et al. (2009), who used the same method of Hm estimation. The season-LT dependence in this study do not agree well with L. Liu et al. (2007), who used electron density profiles from Arecibo ISR between 1966 and 2002. The disagreement may be due to limitations in the calculation method, the data coverage, and inherent dependence of Hm on geographic longitude. They also reported a magnitude of Hm above Korean Peninsula to be in general around 50 km, which is of the same order of magnitude as those in Tulasi Ram et al. (2009) and L. Liu et al. (2007).

In this contribution, observations from the network of Digisonde stations and from Swarm A satellite at middle latitudes, are exploited to calculate the effective scale height in the lower topside ionosphere, and to reveal its characteristics regarding its diurnal variation, its dependence to the altitude and to study its local variability in connection to local plasma irregularities. To this effect, a simplified topside electron density extrapolation model with variable scale height is applied, based on the α-Chapman formulation, referred to here after as α-Chapman – Swarm Digisonde model (α-C-SD model). The model is using as anchor points the ionospheric characteristics in the height of maximum ionization h_mF2, and in the Swarm A altitude. This model provides an estimate of the effective scale height at the Swarm A altitude and its variability during the satellite pass over the Digisonde coincidence area. Comparison of the effective scale height local variability in the coincidence area, with ionogram traces, leads to preliminary conclusions on the propagation of instabilities from the bottomside to the topside ionosphere, indicating the potential to further exploit Swarm and Digisonde data for the development of a model for the effective scale height able to support realistic electron density reconstruction models.

The paper is structured as follows: the data analysis methodology is described in Section 2; the results are presented in Section 3 and discussed in Section 4. Finally, the conclusions and the outlook are presented in Section 5.

2. Data Analysis and Methodology

This section provides details on the data provenance, description and analysis methods. The coincidence criteria between Swarm A and Digisonde stations are defined and the methodology to calculate the topside scale height and identify irregularities in the bottomside and topside ionosphere is described.

2.1. Data

Conditions in the bottomside ionosphere are inferred from the ionograms and ionospheric characteristics provided by the Global Ionospheric Radio Observatory (GIRO) and FastChart databases (Reinisch & Galkin, 2011). All ionograms analyzed in this paper were manually scaled with the SAO Explorer software tool (https://ulcar.uml.edu/SAO-X/SAO-X.html), to minimize the uncertainty in the extracted ionospheric characteristics.

Ionospheric characteristics in the topside are inferred from Swarm A observations, acquired from the VirES database (https://vires.services/). Electric Field Instrument on board Swarm satellites consists of two LP from which the electron density (Ne) can be measured at a rate of 2 Hz (Knudsen et al., 2017). VirES database provides the corrected L1b LP electron density data, as well as the latitude, longitude and altitude of Swarm-A satellite. Time series of the ionospheric plasma irregularities and the total electron content (TEC) with a cadence of 1 Hz were obtained from ESA's Swarm Level 2 products. More information on these products and the access details can be found at: https://earth.esa.int/eogateway/missions/swarm/product-data-handbook/level-2-product-definitions.

Possible offsets in the Swarm LP data have been discussed by Lomidze et al. (2018) who presented calibration and validation results for in situ ionospheric electron density (Ne) and temperature (Te) measured with LP on the three Swarm satellites. The calibration of Swarm A LP data was based on 97 nearly coincident measurements (from December 2013 to June 2016) from low- and middle-latitude ISRs, among which 50 coincidences were identified between Swarm A and the Millstone Hill ISR, while the remaining coincidences were identified with the low-latitude ISR in Arecibo and Jicamarca. The comparison between Swarm A and ISR plasma frequencies indicates that the Swarm LP data are smaller by 9%–11%. Largest discrepancy in the comparison between ISR and Swarm data is seen in frequencies larger than 8 MHz, and in cases of Ne gradients in the equatorial anomaly. Overall, the correlation coefficients are high (≥98%) suggesting very reliable Swarm electron densities. To validate the calibration results, independent measurements were used from equatorial and low-latitude ionosondes. The comparison between the calibrated Swarm A data and the nearly coincident Digisonde plasma frequency at the altitude of the satellite, indicates the validity of the applied correction to the Swarm data. However, a similar validation study could not be performed for the middle latitudes because the ionosphere F region peak altitude is most of the time below the altitude of Swarm A and coincident measurements cannot be identified. Based this analysis, the correction coefficients apply to the low and equatorial region and cannot be considered for the middle latitudes.

We note at this point that the quality of electron density data used in the work presented in this paper, has been checked utilizing all the available information such as the error of the plasma density estimate (Ne_error), the flags indicating the source of measurements (Flags_LP), and the flags characterizing the plasma density measurement (Flags_Ne). In all cases the data were nominal (no missing or suspicious data, the high gain probe has no errors) but errors estimate does not apply or not yet determined (for further information the reader is encouraged to see the associated information at: https://earth.esa.int/eogateway/missions/swarm/product-data-handbook/level-1b-product-definitions).

2.2. Coincidences Between Swarm A and Digisonde Stations

The analysis performed for this paper includes data collected during coincidences of Swarm A satellite with Digisonde stations at middle latitudes within 12 months, from September 2015 to August 2016. The location of Digisonde stations used here is shown in Figure 1.

The Swarm A and Digisonde observations, to be characterized as coincident must meet the following conditions:

1. Spatial condition: collocated observations are considered those acquired within an area centered at the Digisonde station and extends ±2.5° in latitude and longitude. Each satellite pass above the area of coincidence has a maximum duration of almost 78 s (i.e., 156 data points) and a spatial range of 300 km
2. Temporal condition: the ionosondes perform a vertical incidence sounding within in a time interval of few minutes, while 30–90 s are needed to reach the frequency range of the F-region, depending on the time of the day and on the chosen operational parameters. Swarm A observations to be considered as simultaneous with the Digisonde vertical incident ionogram, must be acquired within the duration of ionosonde sounding up to the time the sounder reaches the cut off frequency $foF2$. This condition, to be satisfied, the satellite must enter the coincidence area from 0 to 30 s after the start of the sounding

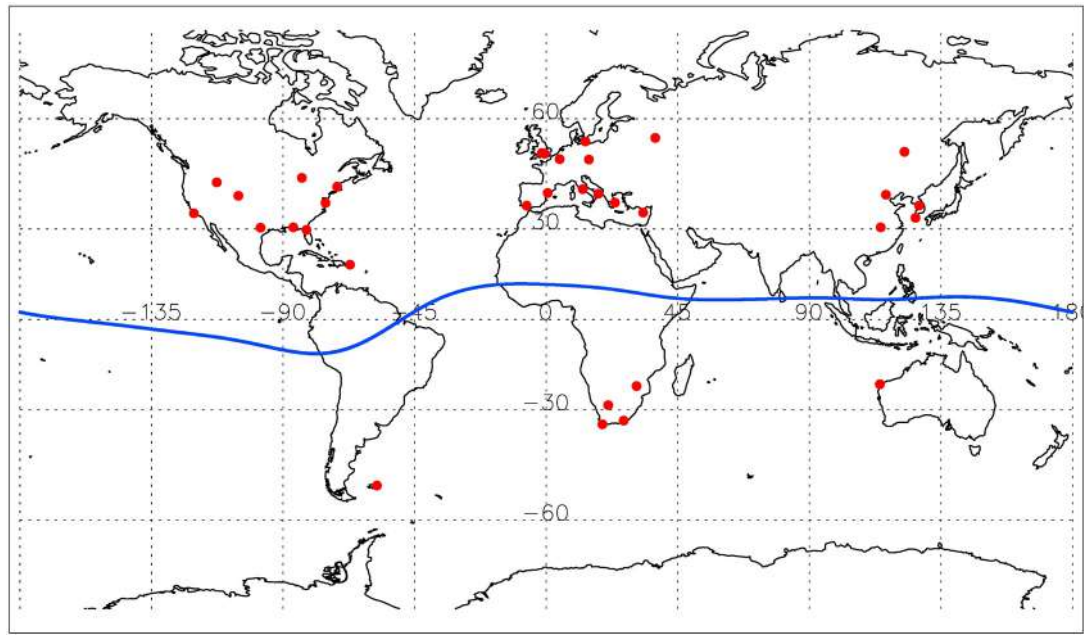

Figure 1. Digisonde data analyzed in this study, are collected from the middle latitude Digisonde stations presented in this map, noted with red circles. The geomagnetic equator is shown with the blue line.

Based on the criteria above, more than 4,000 coincidences have been identified. After performing a quality check on the data, 347 cases were retained for further analysis, among which 125 cases correspond to daytime and nighttime hours and the remaining are coincidences that occurred simultaneously with the solar terminator crossing.

2.3. Evaluation of Ambient Ionospheric Conditions

2.3.1. Large-Scale Disturbances

Background conditions, such as the overall geomagnetic activity can influence the formation of irregularities in the bottomside and topside ionosphere. For the fair assessment of the results, one should consider the ionospheric activity level in the cases under study. To this effect, we compare the relative deviation of the $hmF2$ from the corresponding monthly median ($MhmF2$), calculated as $\frac{hmF2-MhmF2}{MhmF2} \times 100$ with the relative standard deviation (STD) of the median that is used here as an indicator of the normal ionospheric variability (Tsagouri et al., 2018). The relative $STD(\%)$ is calculated as follows:

$$STD(\%) = \frac{STD\_MhmF2}{MhmF2} \times 100$$

where STD_MhmF2 is the standard deviation of the values used for the calculation of the median $hmF2$. Taking into account that the averaged relative deviation is 7.5% and 7% and the relative STD (%) is 9% and 8% during day and nighttime cases, respectively one may argue that the ionospheric variation during the examined cases lies within the normal ionospheric variability. Consequently, the results received are mainly valid under normal ionospheric conditions.

2.3.2. Irregularities

Ionospheric irregularities in the bottomside F-layer, at middle latitudes, are mainly spread F associated with thermospheric gravity waves and related undulations, so called medium-scale traveling ionospheric disturbances (MSTIDs) (Duly et al., 2014; Miller et al., 1997; Saito et al., 2001; Taylor et al., 1998). At middle latitudes, spread F can be of atmospheric or auroral origin.

Spread F has been linked by numerous investigators to a particular plasma instability mechanism thought to operate at middle latitudes attributed to Perkins (1973). Several observational and theoretical investigations associate the mid-latitude spread F with patchy Es layers, although different perspectives exist regarding the

causal relationship (Bowman, 1985; Cosgrove and Tsunoda., 2004; Haldoupis et al., 2003; Hysell et al., 2016; Yokoyama et al., 2009). At middle latitudes, it has been considered that the development of sporadic E layers is due to atmospheric gravity waves, which initiate plasma instabilities.

Spread F appears as scattered echoes in the ionograms. Spread F can manifest as frequency spread F (FF) that are broadened traces that mark reflections from the ionosphere along the frequency axis, or as range spread F (QF) that are along the vertical height axis.

In the review paper by Bowman (1990), a classification of spread F is given according to the corresponding physical mechanisms: frequency spread F (FF) is a medium scale structure with characteristic quasi horizontal trace segments. Range spread F (QF) is due to small-scale structures with characteristic quasi-horizontal patches field-aligned. MSTIDs are large-scale size structures with wavelike characteristics. On the other hand, the relation of the occurrence of spread F to enhancements of the auroral electrojet index (AE) has been studied indicating the occurrence of large-scale traveling ionospheric disturbances (LSTIDs).

In the topside ionosphere Swarm satellites, in their polar orbit, provide in situ electron density observations with its LP experiments. Based on Swarm data, Jin et al. (2019) proposed a set of irregularity indices which are indicative of small, medium and large-scale electron density irregularities in the topside ionosphere: the rate of change of density (ROD), rate of change of density index (RODI), and the large-scale electron density gradient (∇Ne). The large-scale density gradient that corresponds to the spatial scale of 100 km from the satellite (∇Ne_100), is calculated using a linear regression in the running window of 27 data points. At the range of 20 and 50 km two additional density gradient indices are provided (∇Ne_20 and ∇Ne_50). All these Swarm-derived irregularity parameters are sensitive to ionospheric irregularities ranging from mesoscales (10 km) to large scales (100 km), while the phase scintillations from ground-based GPS receivers are sensitive to electron density irregularities of scales ranging from hundreds of meters to several kilometers (Kintner et al., 2007). The range of the electron density gradient (∇Ne) variability is considered in this paper, as an indicator for ionospheric irregularities at the altitude of Swarm A. The correlation of the variability of these indices with the variability of the topside scale height along the satellite pass over a Digisonde, is considered in this paper as a possible indicator of observed irregularities in the topside ionosphere, with a link to the seeded bottomside perturbation.

2.4. Calculation of the Topside Effective Scale Height

Exploiting coincident observations from Swarm A satellite and from Digisonde stations, it is possible to calculate the scale height at Swarm A altitude, adopting a simple reconstruction model up to Swarm A altitude. The reconstruction of the topside electron density profile is based on the assumption that the part of the profile above the altitude of $hmF2$ and up to the altitude of Swarm A (~450 km) follows the α-Chapman model with a variable scale height referred to here after as α-C-SD model. The reconstruction model has two anchor points: the height and electron density at $hmF2$ provided by the Digisonde, and the height and electron density at the topside provided by Swarm A LP experiment. To reconstruct the profile, coincident Swarm A LP observations with Digisonde stations are exploited.

The effective scale height at the Swarm A altitude, H_T, at Swarm A altitude is calculated, assuming that the electron density above the peak height and up to the satellite altitude, follows the α-Chapman approximation described by Equation 1:

$$N_T = NmF2\, exp\left[\frac{1}{2}(1 - z - e^{-z})\right] \tag{1}$$

where

$$z = \int_{hmF2}^{hs} \frac{dh}{H_T} \tag{2}$$

N_T is the Swarm A LP Ne (electron density, m^{-3})

$NmF2$ is the Digisonde derived peak density Ne at $hmF2$

$hmF2$ is the Digisonde derived true height of the peak density (km)

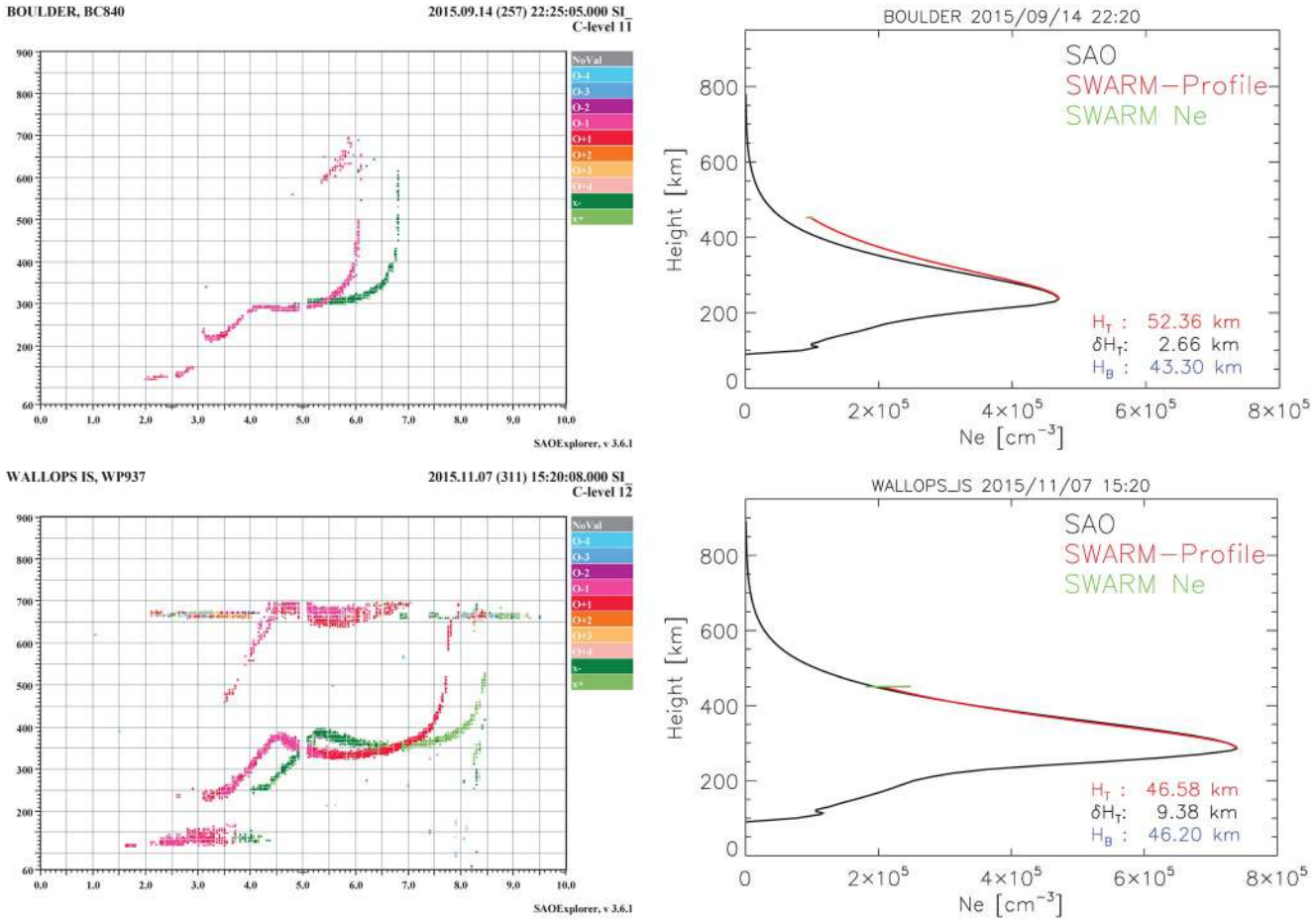

Figure 2. Examples that demonstrate the performance of the topside reconstruction α-C-SD model for daytime ionograms.

hs is the Swarm altitude (km)

The $NmF2$ (in m^{-3}) is calculated from the $foF2$ characteristic (in MHz) using the relationship:

$$NmF2 = 1.24 \times 10^{10} \times foF2^2$$

The effective scale height at the Swarm A altitude, H_T, is calculated for each Swarm A observation during its pass over Digisonde, assuming that the electron density at $hmF2$, remains constant during the satellite pass from the coincident area and equal to $NmF2$ measured by the Digisonde. Obviously, the only unknown parameter in Equations 1 and 2 as described above is the effective scale height H_T. Equations 1 and 2 are solved utilizing a substitution numerical method. In particular, a numerical solution is sought to minimize the difference between the left and the right-hand sides of Equation 1. A solution is assumed of being valid only in the case when the difference is smaller than 0.0001 or the difference is smaller than 0.0001 times $NmF2$. Having calculated the effective scale height H_T at ~450 km, the function of the electron density with altitude can be estimated from the altitude of the $hmF2$ to the altitude of the Swarm A satellite, increasing the altitude by 10 km, to follow the height resolution of the Digisonde measurements and get a continuous electron density profile from the 90 km up to the Swarm A altitude. Indicative cases for the reconstructed electron density profiles with the α-C-SD model are presented in Figure 2 for daytime ionograms and in Figure 3 for nighttime ionograms. In the right-side plot of both figures, two electron density profiles are overplotted:

1. The Digisonde profile (black line) – The electron density profile obtained directly from the SAO file (https://ulcar.uml.edu/~iag/SAO-4.htm); it is important to underline that the topside part is an α-Chapman approximation with constant effective scale height and equal to the effective scale height at the $hmF2$, denoted in the

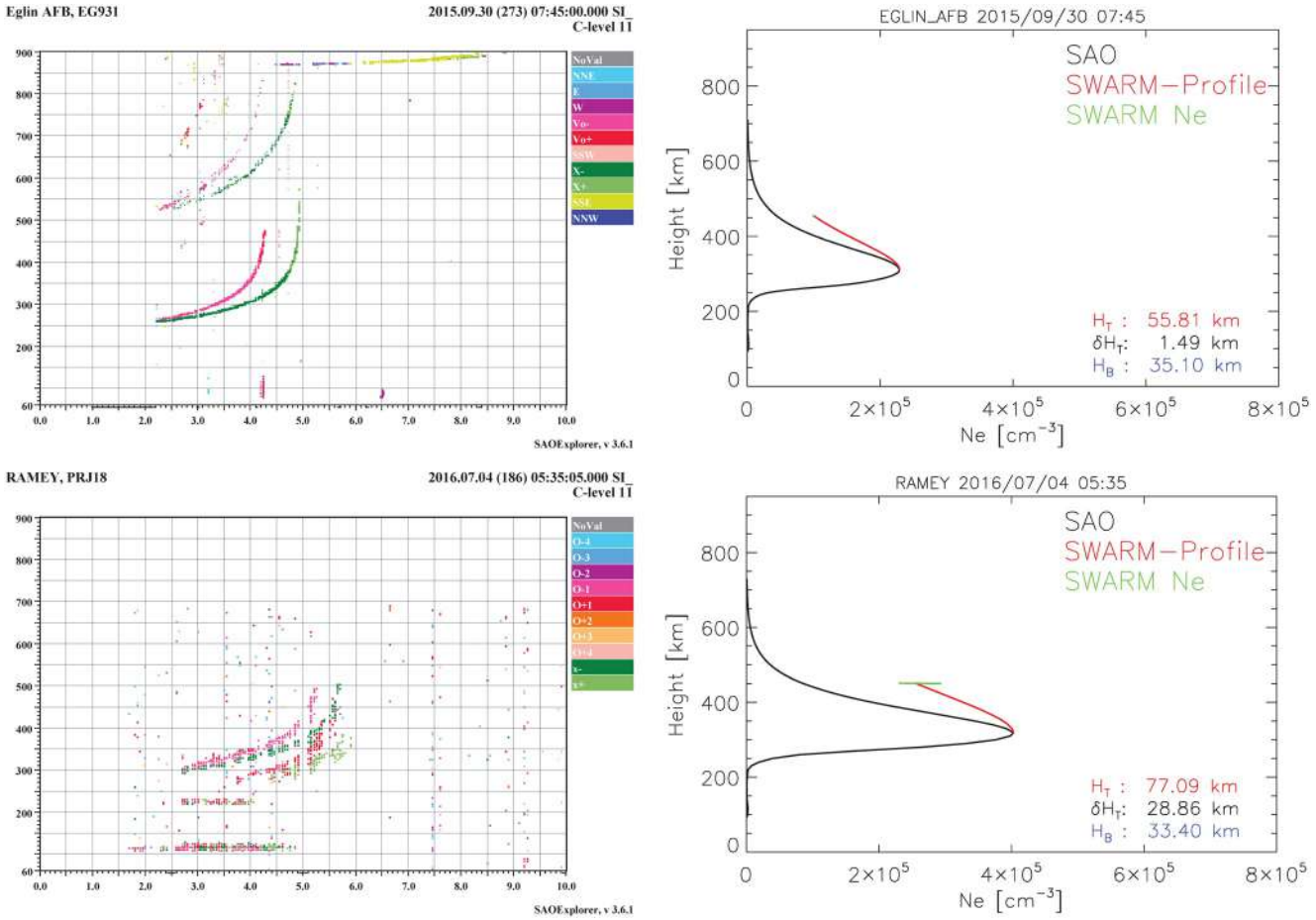

Figure 3. Examples that demonstrate the performance of the topside reconstruction α-C-SD model for nighttime ionograms.

plots as H_B (X. Huang & Reinisch, 2001). This is certainly a simplification, and it is presented here only as a reference topside profile

2. The α-C-SD profile (red line) – The electron density profile obtained at the topside using an α-Chapman function assuming a variable effective scale height which depends on the electron density measured at Swarm A altitude

The Ne characteristic observed from Swarm A LP during its pass along the coincident area (a maximum duration of 78 s), is indicated with the green line in all plots presented in Figures 2 and 3. The mean H_T calculated during the pass of the satellite from the coincidence area, its range δH_T, and the corresponding effective scale height at $hmF2$ (H_B) are given in each of the cases presented in Figures 2 and 3. In three of the cases presented here, the scale height in the topside gets higher values than at $hmF2$. Only for the Wallops Is case, the bottomside and topside effective scale heights have comparable values.

The Boulder ionogram in Figure 2 and the Eglin AFB ionogram in Figure 3 indicate normal stratified ionosphere for daytime and nighttime respectively. For these two cases, the topside scale height values have a range (δH_T) of 2.66 and 1.49 km respectively, or 5% and 3% variability in respect to the mean values. The Wallops Is ionogram (daytime) in Figure 2 and the Ramey ionogram (nighttime) in Figure 3 present spread F conditions with FF = 0.79 and FF = 0.40, respectively. For these two cases, the topside effective scale height calculated during the satellite pass from the coincidence area has a mean value of 46.58 and 77.09 km respectively, with a variability of 20% and 37% in respect to the mean values.

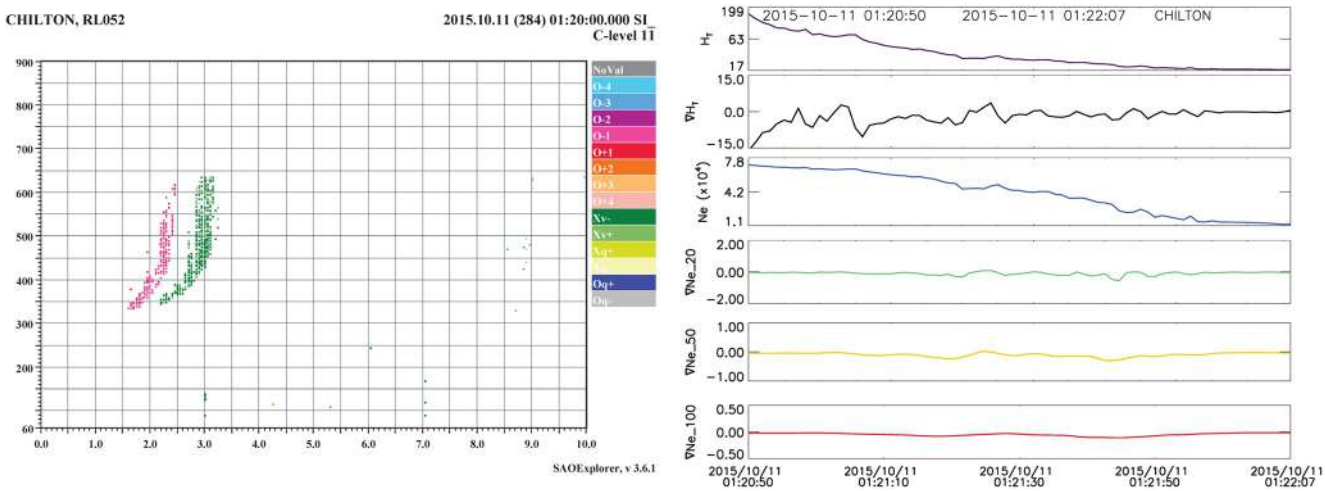

Figure 4. Plots of the scale height H_T (km) and its gradient at the Swarm A altitude, ∇H_T (km/sec), the insitu Swarm A Ne (cm^{-3}) recorded during the satellite pass over the Chilton Digisonde on 11 October 2015 from 01:20:50 UT to 01:22:07 UT, and the corresponding Swarm irregularity indices (∇Ne_20, ∇Ne_50, ∇Ne_100, in cm^{-3}/m), are presented in the plot to the right. The corresponding ionogram from Chilton Digisonde is shown to the left.

The analysis of these examples, provides evidence for possible connection between the spread F occurrence and high variability in the scale height H_T at Swarm A altitude. Consequently, the possibility to consider the variability of H_T as an indicator for the local plasma instability in the topside, is further investigated in Section 3.

3. Results

For all Swarm A/Digisonde coincidences identified using the criteria presented in Section 2.2, the effective scale height H_T at the Swarm A altitude is calculated with the α-C-SC model. The satellite pass over the coincident Digisonde area lasts for 78 s at maximum, an interval that contains at maximum 156 data points from Swarm A LP instrument. For each new Swarm data point, the α-C-SC model provides a new value for the effective scale height H_T at Swarm altitude, assuming that the bottomside ionospheric characteristics, during these 78 s, are constant and equal to the $NmF2$, $hmF2$, and H_B at $hmF2$ extracted from the corresponding ionogram. An example of the topside ionospheric characteristics calculated with this method during Swarm A pass over Chilton Digisonde on 11 October 2015 from 01:20:50 UT to 01:22:07 UT, is presented in Figure 4, together with the corresponding ionogram. The plot to the right presents the effective scale height H_T at the Swarm A altitude calculated with the α-C-SD model, its gradient ∇H_T, the electron density Ne recorded from Swarm LP, and the Swarm Irregularity indices at the range of 20, 50, and 100 km (∇Ne_20, ∇Ne_50, ∇Ne_100).

Given that the conclusions presented hereafter rely largely on the quality and accuracy of the effective scale height calculated with the α-C-SD model, some indicative results on the model performance are provided: To verify the assumption for the α-Chapman approximation from the $hmF2$ to the Swarm A altitude, the model results are compared with independent data. More specifically, the TEC parameter calculated from the UQRG model (Data Courtesy: Manuel Hernandez Pajares, UPC) is compared to the total TEC estimated by the sum of the bottomside TEC (from the Digisonde), plus the topside TEC (from $hmF2$ to the Swarm A altitude), plus the Swarm A TEC, as expressed in Equation 3.

$$Total\,TEC = \int_{90km}^{hmF2} N_{Be}(h)d(h) + \int_{hmF2}^{hs} N_{Te}(h)dh + TEC_S \quad (3)$$

where $N_{Be}(h)$ is the bottomside electron density provided by the Digisonde SAO files, hs is the Swarm altitude, $N_{Te}(h)$ is the reconstructed electron density at the topside using the α-C-SD model, $TECs$ is the vertical TEC calculated between the Swarm A and the GPS satellites.

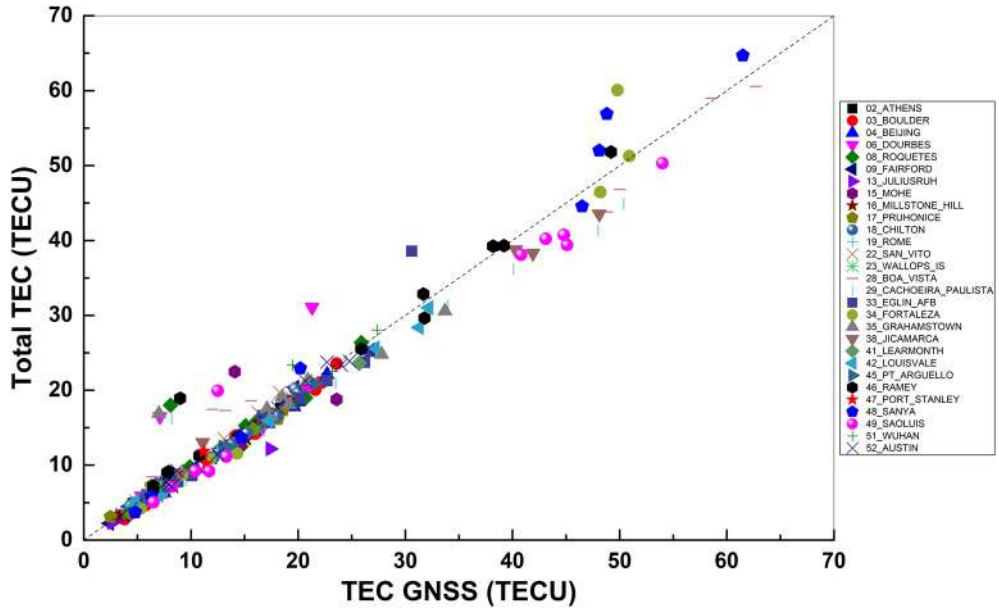

Figure 5. The reconstructed TEC versus the vertical calculated with GNSS data.

The results are presented in Figure 5 and demonstrate that for the large majority of the cases, the reconstructed total TEC is equal to the TEC from UQRG model results (Hernández-Pajares, Roma-Dollase, et al., 2017; Roma-Dollase et al., 2018). This gives us strong evidence that the assumption for the α-Chapman function can well describe the distribution of the electron density of the topside ionosphere not far away from the F layer peak, as previously reported by Stankov et al. (2003). This conclusion agrees with the main outcome from the study published by Pignalberi et al. (2018) who calculated topside effective scale heights by fitting some definite analytical functions (α-Chapman, β-Chapman, Epstein, and exponential) through the values recorded by Swarm and the ones output by the International Reference Ionosphere Update (IRI UP). Calculated effective scale heights were then modeled as a function of $foF2$ and $hmF2$, in order to be operationally applicable to both ionosonde measurements and ionospheric models, like IRI. A statistical comparison with COSMIC/FORMOSAT-3 Radio Occultation profiles was carried out to assess the validity of the proposed method and to investigate which of the considered topside profiles is the best one. The α-Chapman topside function displays the best performance compared to the others and also when compared to the NeQuick topside option of IRI.

In the validation study presented here, the UQRG model results were chosen to provide the ground true, because the model was proven to have the best quality among all the models that provide global ionospheric maps (GIMs). The quality of GIMs against reference TEC derived from GNSS RINEX data has been investigated extensively (Chen et al., 2020; Li et al., 2015). However, one has to keep in mind that the reference GPS TEC is usually based on carrier-to-code leveled (CCL) observations presenting the accuracy of 2–10 TECU depending on station latitude and solar activity (Brunini & Azpilicueta, 2010; Ciraolo et al., 2007). Recently, Wielgosz et al. (2021) evaluated the accuracy of eight GIMs including the UQRG model, using two different methods, the self-consistency analysis and comparison to altimetry TEC data. With both methods, the UQRG model was characterized by the lowest annual root mean square (RMS) for low and high level of solar flux and for different geomagnetic regions (low, middle, and high latitudes). In the validation study by Wielgosz et al. (2021), UQRG is the only model that obtained an annual STD below 4 TECU. It is clear that in the validation presented in Figure 5, the use of UQRG model supports the consistent reproduction of TEC for all different geographic locations and solar activity, with a STD comparable and even lower than the STD from reference TEC derived from RINEX data.

The results extracted from all coincidences included in this study, are used to investigate the diurnal variation of the effective scale heights at $hmF2$ and at the Swarm A altitude (lower part of the topside ionosphere). The diurnal variation with Local Time for the two characteristics is presented in Figure 6. The average value with its standard deviation is calculated based on all the coincidences identified within each hour of the day. The bottomside scale height H_B exhibits a daily variation with the higher values around noon time. On the contrary, the daily

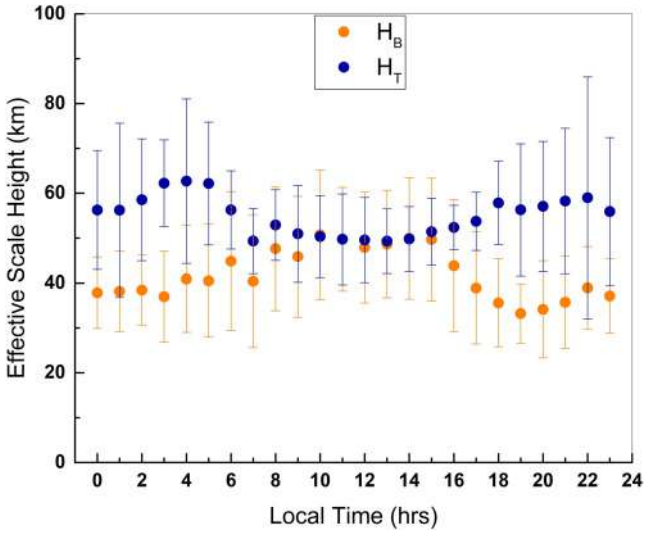

Figure 6. The average value and the standard deviation of the bottomside and the topside effective scale heights calculated based on all the coincidences identified within the hour in Local Times.

variation pattern of the topside scale height H_T, exhibits two maxima – one in the early morning and another in the evening hours. At nighttime hours, the effective scale height in the topside is in general larger than at $hmF2$, which indicates a trend for an increase with altitude above the $hmF2$. During daytime hours, the two scale heights have comparable magnitudes.

In the analysis that follows, the mean value of the topside effective scale height H_T is calculated for each Swarm A pass over Digisonde, with its gradient ∇H_T, and it is compared with the effective scale height at the $hmF2$, H_B provided by coincident Digisonde manually scaled ionograms. The results are shown in Figure 7 grouped by nighttime and daytime cases. Here the cases that correspond to the crossing of the solar terminator are excluded. The top panels show the variation of the bottomside effective scale height (orange-colored symbols) and of the topside effective scale height (blue-colored symbols) as a function of the Swarm A distance from $hmF2$. The range of the effective scale height variability is marked with vertical bars. The bottom panels in Figure 7, present the frequency spread (FF) with blue symbols and the range spread F (QF) with orange symbols versus the distance of the satellite from the height of the peak electron density, that is, from $hmF2$. This graphical representation intends to provide information about the irregularities in the bottomside, recorded while Swarm A was passing over the Digisonde stations.

The first remark is that the Swarm A distance from the $hmF2$ is always positive, confirming that the satellite is always at the topside, for the cases considered in this analysis.

Regarding the mean value of the effective scale height H_T calculated during the satellite pass over the Digisonde coincident area, Figure 7 indicates that for the nighttime cases, the mean H_T is comparable to the bottomside

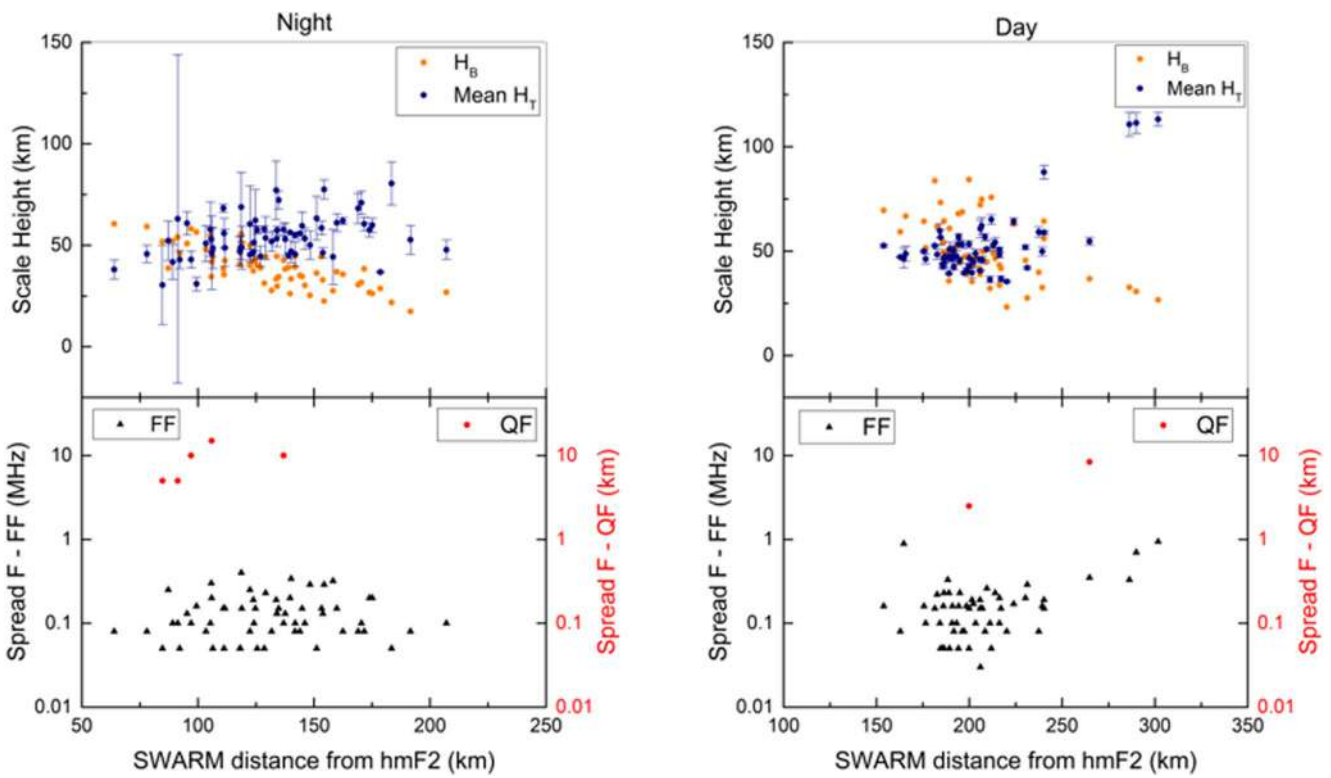

Figure 7. Scale Height as a function of the satellite distance from h_mF2, under nighttime and daytime Swarm-Digisonde coincidences.

scale height H_B when $hmF2$ distance from Swarm A is smaller than ~120 km. For larger distances, that is, when the h_mF2 drops below 330 km, the bottomside scale height decreases and deviates significantly from the topside scale height values. During daytime passes, and for short distance of $hmF2$ from Swarm A (less than 200 km), the bottomside scale height H_B tends to be larger than the topside scale height H_T. As the $hmF2$ drops to lower altitudes, the effective scale height at Swarm A altitude becomes larger than the effective scale height at $hmF2$. The cases for which Swarm A distance from $hmF2$ is very large, are only a few and are considered to be extreme cases. For all these extreme cases, the range of the topside scale height variability is considerably large, while strong spread F is observed in the corresponding ionograms. Overall, there is a linear positive trend for the effective scale height to increase above the level of the $hmF2$ in nighttime cases. However, in the daytime cases, the linear trend is not obvious especially if the extreme cases are excluded. A complex behavior is rather observed with the two characteristics competing each other in magnitude. As pointed out by Park et al. (2015), statistical distributions of the topside scale height, revealed from the analysis of Swarm scale height over Korea, exhibited a complex dependence upon local time and season. This does not fully agree with the general concept for a linear increase of the scale height with altitude above the height of the peak density.

To summarize the observations from Figures 6 and 7:

1. For the nighttime cases, the topside effective scale height at 450 km altitude, has a mean value of ~56 km and is higher than the effective scale height at $hmF2$. At local spatial scales, its variability is higher when the satellite is closer to the height of the peak density $hmF2$. When the $F2$ layer drops to lower altitudes, the bottomside scale height is decreasing and its magnitude deviates from the effective scale height at Swarm A location
2. For daytime cases, the effective scale height variability at 450 km has a mean value of ~52 km and gets general lower values compared to the nighttime cases; its mean value is comparable to the scale height at $hmF2$ only when the distance of Swarm A from $hmF2$ is short and up to 250 km. When $hmF2$ drops further down, the magnitude of the topside and bottomside effective scale height deviate significantly
3. The bottomside effective scale height exhibits a diurnal variation with its maximum around noon. The diurnal pattern of the topside effective scale height at ~450 km presents two maxima in the early morning and evening hours

Regarding the local variability of the scale height at Swarm altitude within the 78 s of the satellite pass from the coincidence area, it is noticed from Figure 7 that the variability at night is significantly higher than the variability in the daytime passes. Given that the ionospheric irregularities in the bottomside are observed more often at night (Bowman, 1992), a more detailed analysis is attempted to investigate the relation of the irregularities recorded in the bottomside ionosphere with the variability of the effective scale height in the topside.

Frequency spread F is observed in 55 cases at daytime among which only in 11 cases, FF $\geq$ 0.2 and in 60 cases at nighttime ionograms among which only in 20 cases, FF $\geq$ 0.2. Range spread F is observed in five cases in the nighttime ionograms and in two cases in daytime ionograms. These numbers show that conditions regarding the spread F occurrence are not very different between the daytime and nighttime cases considered here. Therefore, rather than analyzing the statistical behavior, individual cases are studied. These cases demonstrate the high variability of the effective scale height at Swarm A altitude during its 78 s passes from the coincidence areas while strong spread F is recorded in the bottomside ionograms, and are shown in Figure 8 for nighttime cases and in Figure 9 for daytime cases.

The irregularities detected in the ionograms shown in Figure 8, are due to spread F medium scale irregular structures while for the Boulder case (22 October 2015) range spread F (QF) is also detected. The variability of the effective scale height (∇H_T) is stronger for the Boulder case, and weaker for the Millstone Hill case. For both cases the variability pattern of the effective scale height gradient shows a good agreement with the ∇Ne_20 km, less good agreement with ∇Ne_50 km and practically no agreement with ∇Ne_100 km. This provides some evidence that the medium scale irregularities formed in the bottomside ionosphere, as they propagate upwards, break into smaller structures and appear as plasma irregularities with the small spatial scale of 20 km.

The irregularities detected in the daytime ionograms shown in Figure 9, are due to MSTIDs. For these cases the variability pattern of the effective topside scale height (∇H_T) does not show an agreement with any of three ∇Ne Swarm irregularity indices. MSTIDs are usually observed few minutes before the commencement

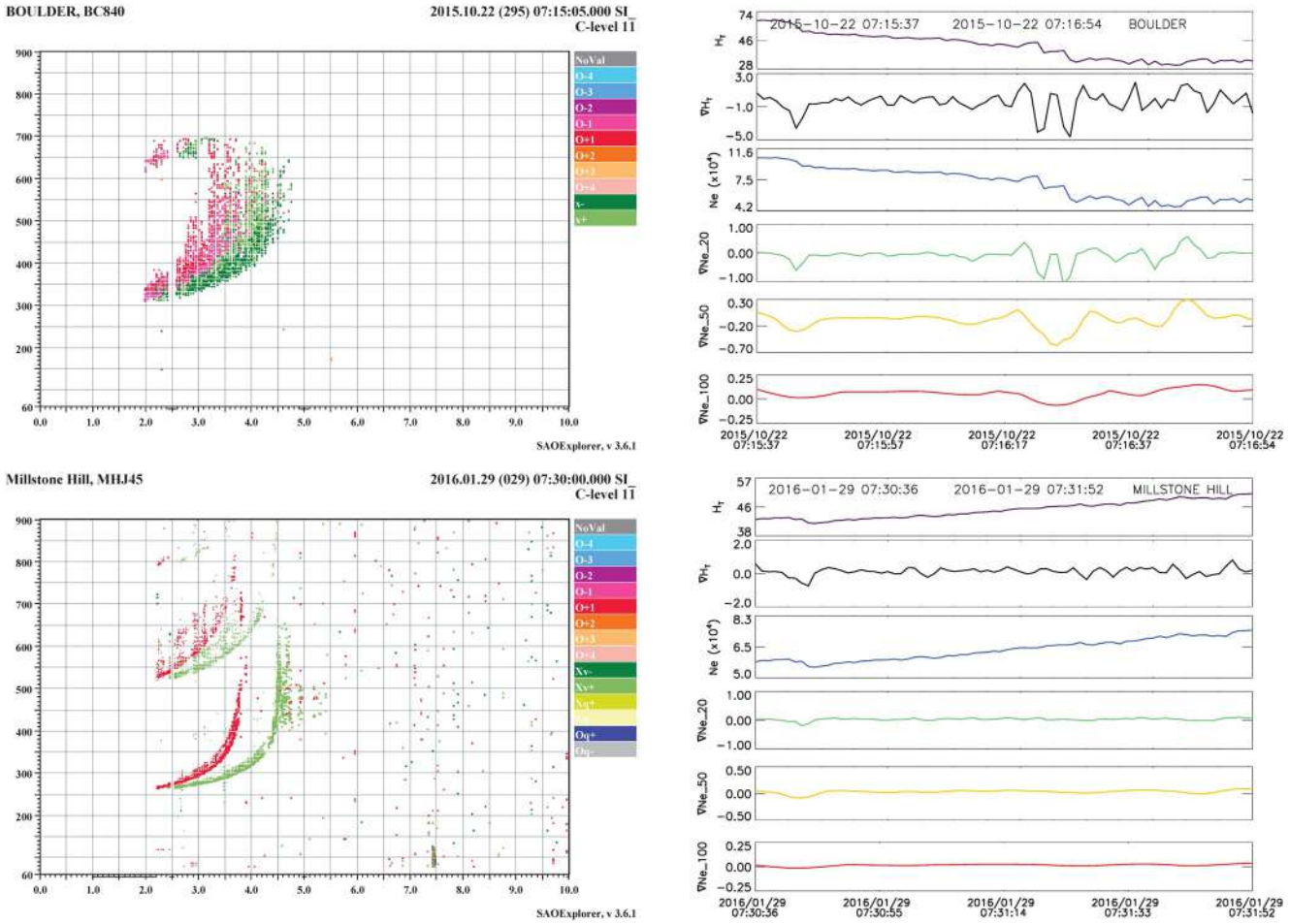

Figure 8. Nighttime ionograms and the corresponding Swarm A coincident data, presented in the same format as described in Figure 4.

of spread F. After the passage of TIDs, the perturbation grows to break into small-scale structures before it can be spread into the topside region. The time needed for this cascade, is enough for the satellite to move outside the coincidence area, and this probably explains the unrelated data of the (∇H_T) and the Swarm irregularity indices.

Table 1 provides a list of indicative Swarm A/Digisonde coincidences with the estimated correlation coefficients between the gradient of the effective Scale Height at Swarm A altitude and the Swarm ∇Ne irregularity indices, together with an indication for the prevailing conditions in the bottomside ionosphere and the numerical values estimated for the effective scale heights H_B and H_T. The results indicate that there is a trend for good agreement between the gradient of the effective scale height at Swarm altitude (∇H_T) and the Swarm irregularity index at the range of 20 km (∇Ne_20 km) only when irregularities of small and medium size are recorded in the bottomside ionosphere as FF and QF spread F. In all other cases (normal stratification or MSTIDs) the scale height gradient varies independently from the Swarm irregularity indices. Furthermore, for the cases when strong spread F is recorded, the variability of the H_T along the trajectory of the satellite over the coincidence area, is much higher than in the rest of the cases.

The Swarm irregularity indices, from their definition, are dependent only on the local electron density perturbation detected by Swarm LP instrument. The topside effective scale height depends on both the bottomside electron density at $hmF2$ and on the local electron density at Swarm A altitude. Therefore, perturbations in the bottomside ionosphere are reflected in the topside effective scale height and its variability ∇H_T. The correlation between ∇H_T and ∇Ne_r indices indicates that the same source of perturbation affects simultaneously the bottomside and its

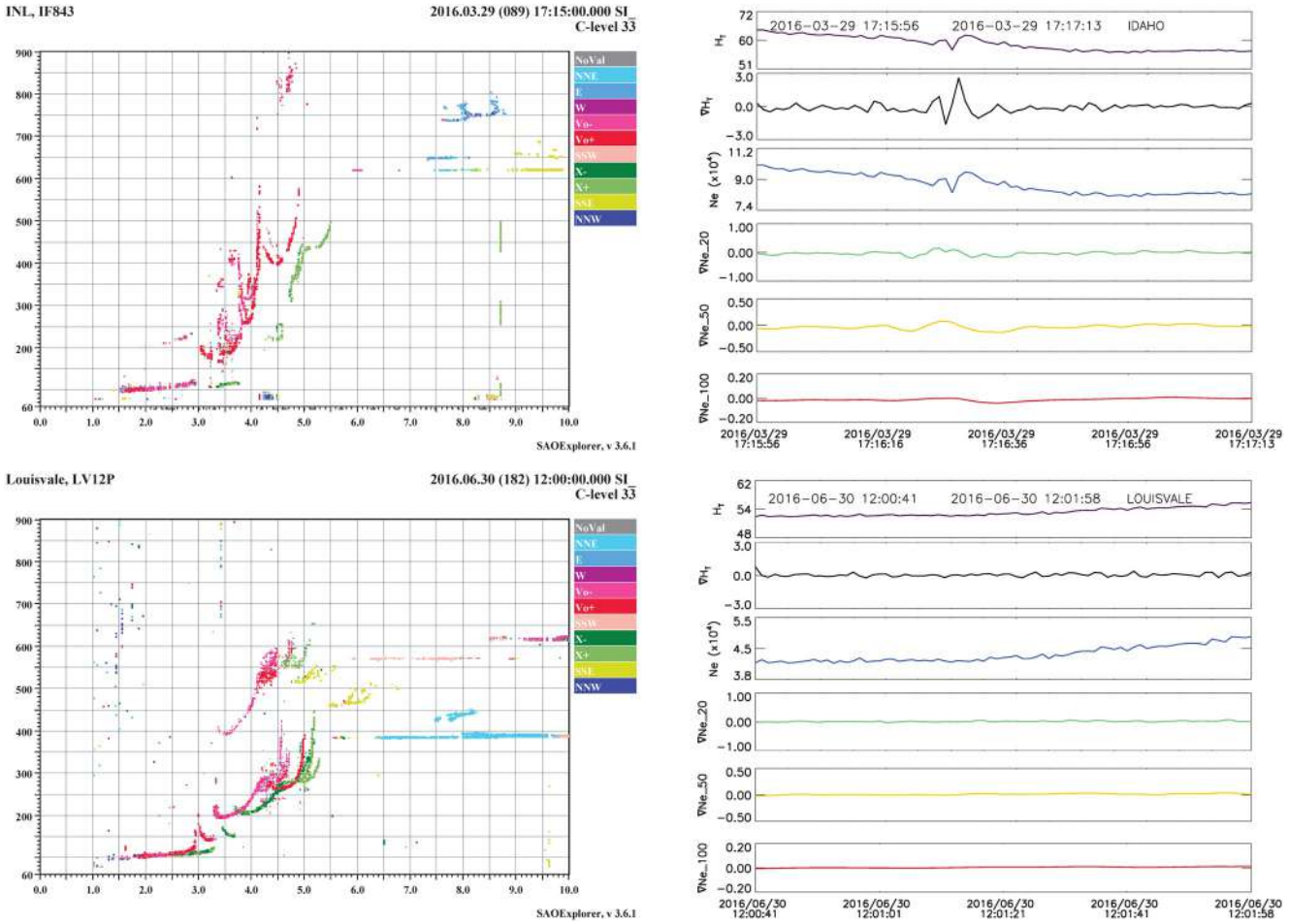

Figure 9. Same as Figure 8 for daytime ionograms.

overhead topside ionosphere. The fact that the best correlation is found only for the range of 20 km indicates that the irregularities as moving upwards, are cascaded to small structures.

4. Discussion

In this paper we attempt to specify characteristics of the effective scale height at the lower layers of the topside ionosphere, extracted from coincident Swarm A electron density data and vertical incidence ionograms from Digisonde stations at middle latitudes. The analysis reports preliminary results that concern the time interval from September 2015 to August 2016. The coincidence is defined based on spatial and the temporal criteria to verify that Swarm A observations were acquired within the time interval of a vertical incidence sounding, and while the satellite was passing above the ionospheric station. Based on these criteria 347 coincidences were identified during the 12 months of data coverage covering all Local Times. All sampled Digisonde data have been manually scaled and the extracted ionospheric characteristics $foF2$, $hmF2$, and H_B, have been used to reconstruct the topside electron density profile up to Swarm A altitude with the α-C-SD model.

The present analysis does not reveal a systematic relation between the two effective scale heights H_B and H_T. While during nighttime, early morning and evening hours the condition $H_B < H_T$ is met, during daytime the two characteristics the magnitudes of the two characteristics compete each other. The conclusion extracted from this preliminary analysis is that although the effective scale height above the $hmF2$, tends to increase with altitude, in several cases the relation between H_B and H_T is much more complex.

Table 1
Indicative Swarm/Digisonde Coincidences With the Prevailing Bottomside Conditions, the Estimated Effective Scale Heights at hmF2 (H_B) and at the Swarm A Altitude (H_T) and the Correlation Coefficients Between the Gradient Scale Height H_T and the Swarm Irregularity Indices ∇Ne_r at Three Different Ranges 20, 50, and 100 km

						Correlation coefficients between the ∇H_T and ∇Ne_r		
URSI code	Digisonde name	Coincidence start time	Bottomside conditions	H_B (km)	H_T (km)	r = 20 km	r = 50 km	r = 100 km
EG931	EGLIN	30/09/2015 07:45:45	FF = 0.08	35.1	55.8 ± 1.5	0.381	0.397	0.321
RL052	CHILTON	22/03/2016 10:40:47	FF = 0	48.3	54.0 ± 5.1	0.471	0.411	0.085
BC840	BOULDER	14/09/2015 22:25:00	FF = 0.05	43.3	52.4 ± 2.7	0.510	0.388	0.205
IF843	IDAHO	29/03/2016 17:15:56	MSTID	71.1	61.6 ± 8.9	0.422	0.314	0.302
LV12P	LOUISVALE	30/06/2016 12:00:41	MSTID	37.6	55.5 ± 3.9	0.239	0.141	0.134
BC840	BOULDER	22/10/2015 07:15:37	FF = 0.20 QF = 15	41.8	46.2 ± 36.2	0.829	0.569	0.422
WP937	WALLOPS_IS	07/11/2015 15:20:37	FF = 0.79	72.1	30.9 ± 5.6	0.850	0.780	0.745
MHJ45	MILLSTONE HILL	02/08/2016 03:15:42	FF = 0.27	19.9	58.4 ± 17.2	0.826	0.704	0.560
PRJ18	RAMEY	04/07/2016 05:35:27	FF = 0.40	19.5	76.9 ± 28.8	0.890	0.813	0.754
MHJ45	MILLSTONE HILL	29/01/2016 07:30:36	FF = 0.23	35.2	47.2 ± 11.1	0.761	0.682	0.511

The relative variation of the effective scale height in the topside, in respect to the effective scale height at the *hmF2* altitude, shows that within a layer of 120 km at night and 250 km at daytime above the *hmF2*, the effective scale height does not vary considerably. This indicates that in the F2 layer the ionospheric plasma is relatively stable within this range, mainly affected by the thermospheric temperature that determines the bottomside parameters and consequently, the scale height at *hmF2* (Belehaki et al., 2006). In addition, this result supports the conclusion that the effective scale height is considered to be a measure of the topside thickness of the ionosphere (Gulyaeva, 2007), and of the slab thickness (e.g., Goodwin et al., 1995; Jayachandran et al., 2004).

Linear dependence of the effective scale height with the altitude in the topside ionosphere has been previously reported (Hernández-Pajares, Garcia-Fernández, et al., 2017) and potentially attributed to an imbalance between the extreme ultraviolet (EUV) flux and the cooling scale time of electrons (Olivares-Pulido et al., 2016; Su et al., 2015). Such imbalance would yield a systematic increase of the scale height with altitude, consistently with the corresponding increase of the electron temperature in this ionospheric region.

On a local scale, the comparison between irregularities in the bottomside ionosphere and perturbations in the topside detected as local Ne and scale height gradients, provides evidence for possible connection between bottomside and topside irregularities.

The high correlation between the gradient of the effective scale height in the topside and the Swarm irregularity indices at the range of 20 km, when the bottomside ionograms record spread F, supports the scenario for the small to medium scale irregular structures to break into even smaller scale plasma patches of 20 km scales, as they propagate to the topside ionosphere.

Originally, ionospheric instabilities have identified in the low and high magnetic latitudes, while the ionosphere at mid-latitudes was considered to be stable. In fact, the middle latitude zone is not subject to strong forcing from the magnetosphere as at auroral latitudes. Furthermore, at the equatorial latitudes the nearly horizontal magnetic field lines support the ionosphere against gravity, a condition which favors the generation of plasma interchange instabilities. Nevertheless, many studies have reported midlatitude ionospheric irregularities triggered from below associated with tsunami (Savastano et al., 2017), convective storms (Makela et al., 2006), hurricanes (Bishop et al., 2006), earthquakes (J. Y. Liu et al., 2011), meteors (Chernogor, 2015), and explosions (Fitzgerald, 1997). This type of instabilities was first observed in the bottomside ionosphere, which is explained with the Gravitational Rayleigh-Taylor (GRT) theory, because of the upward electron density gradient. One of the problems was the detection of irregularities in the stable topside ionosphere where the electron density gradient is downward. This problem was resolved by Woodman and La Hoz (1976) who discovered the plume-like

features from digital range-time-intensity (RTI) plots developed using Jicamarca radar results, demonstrating the clear connection between topside irregularities and the bottomside energy source of the topside irregularities. Later on, Kelly et al. (1981) and Woodman (1993) analyzing the evolution of a bubble, discovered a clear wavy shape in the bottomside ionosphere that became completely irregular in the upper part of the bubble. In the region between these two ends, there was a transition phase from wave structure to total irregular structure. The penetrations of the upwelling plasma bubbles into the topside ionosphere have been reproduced by numerical simulations (Chou & Kuo, 1993, 1996; C. S. Huang & Kelley, 1996a, 1996b, 1996c; Ossakow, 1981; Zalesak et al., 1982; Zalesak & Ossakow, 1980) that all agree that the penetration is a nonlinear process in the stable topside ionosphere. Kuo et al. (1998) investigated the cascading process of the bubble from wave structure into irregularities. In contrast to the topside ionospheric irregularities, which are originated in the distant bottomside ionosphere, the bottomside ionospheric irregularities are originated from right where they are, without spreading to the nonperturbed region. Therefore, the seeded perturbation is very probably limited to a finite region where the growth of the perturbation is so fast that the perturbation grows in a short time to break into many small-scale structures before it can spread to the nonperturbed region. To explain this mechanism, Kuo et al. (1998) proposed that the existence of a strong neutral wind jet superposed by seeding gravity waves in the bottomside ionosphere may generate and confine the irregularities in a limited height range. It was proven that the neutral wind jet is an excellent condition in which to confine the bottomside irregularities because it has a strong vertical wind shear which provides a large height range of dynamic instability. The atmospheric gravity wave tends to propagate upward freely. When it reaches the height of the critical level, where the horizontal phase velocity of the gravity wave matches the wind speed, the wave will be stopped from propagating farther upward with its wave amplitude of the horizontal component growing because of dynamic instability and the vertical wavelength as well as the wave amplitude of the vertical component decreasing with height as it approaches the critical level (C. M. Huang et al., 1992; Kuo et al., 1992; Kuo & Lue, 1994). Therefore, the neutral wind jet can trap gravity waves of different horizontal phase velocities with very large amplitudes and very small vertical wavelengths in a limited range of height. Furthermore, these trapped gravity waves will continually grow to cascade into smaller-scale waves in the vicinity of the critical level: the stronger the vertical wind shear, the faster the cascading process; and the faster the cascading process, the smaller the chance of perturbation leakage.

Recent work (Eltrass et al., 2014, 2016) finds that the temperature gradient instability is likely responsible for the cascading of irregularity structure sizes in the decameter regime at midlatitudes.

Hysell et al. (2018) shown observations of mid-latitude F-region plasma density irregularities occurring in tandem with Es-layer irregularities over Arecibo during a geomagnetically quiet period. The morphology of the irregularities together with quantitative information about the underlying plasma state and dynamics are captured precisely in the Arecibo data. Previous measurements of mid-latitude spread F at Arecibo and elsewhere have suggested wavelike variations in the height of the F-layer peak. The observations presented by Hysell et al. (2018) are unique in that they show much deeper instability with significant upwelling and overturning in plasma density extending well into the topside. Numerical simulation results of the midlatitude ionosphere have used to explain the most important features in the Arecibo observations including the patchy Es layers, MSTIDs, bottomside spread F irregularities, and irregularities in the topside. The most important ingredient in the simulations are intense gravity waves propagating upward into the thermosphere. The gravity wave wind fields both form the Es layers and cause them to structure, induce MSTIDs through dynamo action, and drive currents in the F region which lead to the formation of bottomside irregularities. Most importantly, the gravity waves induce electric fields in the E region which map along magnetic fields into the topside where they produce irregularities in the topside through convection and advection.

5. Conclusions and Outlook

1. The α-C-SD model provides the reconstructed topside electron density profile up to the altitude of ~450 km, based on the α-Chapman function and on coincident Swarm and Digisonde data. This approach assumes a reconstruction with variable scale height, having two anchor points, at $hmF2$ and at Swarm A altitude. Given that the validation of the method provides a good agreement between the modeled TEC and the calculated TEC, it is confident to assume for the α-C-SD model reliability and exploit further the estimated effective scale height at Swarm A altitude for the purposes of this analysis

2. The effective scale height at middle latitudes above the height of the peak electron density remains relatively stable during the daytime hours around the local noon, while in the nighttime, early morning and evening sectors an increase with the altitude is inferred from the data analyzed here that cover the period from September 2015 to August 2016
3. The gradient of the topside effective scale height during the satellite pass over the Digisonde station, can be considered as an indicator for small-scale irregularities in the topside. These irregularities are simultaneously detected by the Swarm ∇Ne_20 index that corresponds to irregular plasma structures at the topside at the range of 20 km. This conclusion indicates the irregularities as moving upwards, are cascaded to small structures
4. Medium and large-scale irregularities at the range of 50 and 100 km represented by the two Swarm irregularity indices ∇Ne_50 and ∇Ne_100, could not be correlated to any type of bottomside irregularity structures detected in the sample of data examined for this paper

The results presented here are based on preliminary conclusions extracted from 12 months of Digisonde and Swarm A observations. Therefore, these results are indicative for certain features and cannot be considered to be statistically significant. Further analysis is required with more data in order to confirm their validity. The analysis is being expanded to cover a larger time period and to include coincidences with Swarm A and Swarm B satellites, in order to build a reliable model for the effective scale height variation with local time, altitude and latitude and study in more depth the relation between the local effective scale height variability with plasma irregularities. Such a model should be able to support the development of realistic electron density reconstruction models.

Data Availability Statement

The Swarm A electron density data used in this paper are available in the VirES database (https://vires.services/). The time series of the Swarm TEC and ionospheric plasma irregularity indices were retrieved from the ESA's Swarm Level 2 products database (https://earth.esa.int/eogateway/missions/swarm/product-data-handbook/level-2-product-definitions). The Digisonde ionograms and SAO files were retrieved from the GIRO (https://giro.uml.edu/index.html) and FastChart (https://giro.uml.edu/didbase/scaled.php) databases. The GNSS TEC data used for the validation of the α-C-SD model were kindly made available by Prof. Manuel Hernandez-Pajares (UPC, Spain) using his UQRG model.

Acknowledgments
The study was funded from COSTO project, which has received funding from the ESA contract 4000126730/19/NL/IA, in the framework of the "Swarm + Coupling: High-Low Atmosphere Interactions" Call. A. Belehaki acknowledges financial support provided by the AFRL grant award FA9550-19-1-7019 and by the PITHIA-NRF Horizon 2020 Grant Agreement 101007599 of the European Commission.

References

Belehaki, A., Jakowski, N., & Reinisch, B. W. (2003). Comparison of ionospheric ionization measurements over Athens using ground ionosonde and GPS-derived TEC values. *Radio Science*, *38*(6), 1105–1116. https://doi.org/10.1029/2003RS002868

Belehaki, A., Marinov, P., Kutiev, I., Jakowski, N., & Stankov, S. (2006). Comparison of the topside ionosphere scale height determined by topside sounders model and bottomside Digisonde profiles. *Advances in Space Research*, *37*(5), 963–966. https://doi.org/10.1016/j.asr.2005.09.014

Bishop, R. L., Aponte, N., Earle, G. D., Sulzer, M., Larsen, M. F., & Peng, G. S. (2006). Arecibo observations of ionospheric perturbations associated with the passage of tropical Storm Odette. *Journal of Geophysical Research*, *111*, A11320. https://doi.org/10.1029/2006JA011668

Bowman, G. G. (1985). Some aspects of mid-latitude spread-Es, and its relationship with spread-F. *Planetary and Space Science*, *33*, 1081–1089. https://doi.org/10.1016/0032-0633(85)90027-3

Bowman, G. G. (1990). A review of some recent work on mid-latitude spread-F occurrences as detected by ionosondes. *Journal of Geomagnetism and Geoelectricity*, *42*, 109–138. https://doi.org/10.5636/jgg.42.109

Bowman, G. G. (1992). Upper atmosphere neutral-particle density variations compared with spread-F occurrence rates at locations around the world. *Annales de Geophysique*, *10*, 676–682.

Brunini, C., & Azpilicueta, F. (2010). GPS slant total electron content accuracy using the single layer model under different geomagnetic regions and ionospheric conditions. *Journal of Geodesy*, *84*(5), 293–304. https://doi.org/10.1007/s00190-010-0367-5

Chen, P., Liu, H., Ma, Y., & Zheng, N. (2020). Accuracy and consistency of different global ionospheric maps released by IGS ionosphere associate analysis centers. *Advances in Space Research*, *65*(1), 163–174. https://doi.org/10.1016/j.asr.2019.09.042

Chernogor, L. F. (2015). Ionospheric effects of the Chelyabinsk meteoroid. *Geomagnetism and Aeronomy*, *55*(3), 353–368. https://doi.org/10.1134/S0016793215030044

Chou, S. Y., & Kuo, F. S. (1993). Simulation of neutral wind field effect on equatorial spread F. In F.-S. Kuo (Ed.), *Low-latitude ionospheric physics*. *COSPAR Colloq*. Ser. (Vol. 7, pp. 83–95). Elsevier Science.

Chou, S. Y., & Kuo, F. S. (1996). A numerical study of the wind field effect on the growth and observability of equatorial spread F. *Journal of Geophysical Research*, *101*, 17137–17149. https://doi.org/10.1029/96ja01404

Ciraolo, L., Azpilicueta, F., Brunini, C., Meza, A., & Radicella, S. M. (2007). Calibration errors on experimental slant total electron content (TEC) determined with GPS. *Journal of Geodesy*, *81*(2), 111–120. https://doi.org/10.1007/s00190-006-0093-1

Cosgrove, R. B., & Tsunoda, R. T. (2004). Instability of the E-F coupled nighttime midlatitude ionosphere. *Journal of Geophysical Research*, *109*. https://doi.org/10.1029/2003JA010243

dos Santos Prol, F., Themens, D. R., Hernández-Pajares, M., de Oliveira Camargo, P., & de Assis Honorato Muella, M. T. (2019). Linear vary-chap topside electron density model with topside sounder and radio-occultation data. *Surveys in Geophysics*, *40*, 277–293. https://doi.org/10.1007/s10712-019-09521-3

Duly, T. M., Huba, J. D., & Makela, J. J. (2014). Self-consistent generation of MSTIDs within the SAMI3 numerical model. *Journal of Geophysical Research*, *119*, 6745–6757. https://doi.org/10.1002/2014ja020146

Eltrass, A., Mahmoudian, A., Scales, W. A., de Larquier, S., Ruohoniemi, J. M., Baker, J. B. H., et al. (2014). Investigation of the temperature gradient instability as the source of midlatitude quiet time decameter-scale ionospheric irregularities: 2. Linear analysis. *Journal of Geophysical Research: Space Physics*, *119*, 4882–4893. https://doi.org/10.1002/2013JA019644

Eltrass, A., Scales, W. A., Erickson, P. J., Ruohoniemi, J. M., & Baker, J. B. H. (2016). Investigation of the role of plasma wave cascading processes in the formation of midlatitude irregularities utilizing GPS and radar observations. *Radio Science*, *51*, 836–851. https://doi.org/10.1002/2015RS005790

Fitzgerald, T. J. (1997). Observations of total electron content perturbations on GPS signals caused by a ground level explosion. *Journal of Atmospheric and Solar-Terrestrial Physics*, *59*(7), 829–834. https://doi.org/10.1016/S1364-6826(96)00105-8

Goodwin, G. L., Silby, J. H., Lynn, K. J. W., Breed, A. M., & Essex, E. A. (1995). GPS satellite measurements: Ionospheric slab thickness and total electron content. *Journal of Atmospheric and Terrestrial Physics*, *57*(14), 1723–1732. https://doi.org/10.1016/0021-9169(95)00093-h

Gulyaeva, T. (2007). Variable coupling between the bottomside and topside thickness of the ionosphere. *Journal of Atmospheric and Solar-Terrestrial Physics*, *69*, 528–536. https://doi.org/10.1016/j.jastp.2006.10.015

Haldoupis, C., Kelley, M. C., Hussey, G. C., & Shalimov, S. (2003). Role of unstable sporadic-E layers in the generations of midlatitude spread. *Journal of Geophysical Research*, *108*, 1446. https://doi.org/10.1029/2003ja009956

Hernández-Pajares, M., Garcia-Fernàndez, M., Rius, A., Notarpietro, R., von Engeln, A., Olivares-Pulido, G., et al. (2017). Electron density extrapolation above F2 peak by the linear Vary-Chap model supporting new Global Navigation Satellite Systems-LEO occultation missions. *Journal of Geophysical Research: Space Physics*, *122*, 9003–9014. https://doi.org/10.1002/2017JA023876

Hernández-Pajares, M., Roma-Dollase, D., Krankowski, A., GarcíaRigo, A., & Orús-Pérez, R. (2017). Methodology and consistency of slant and vertical assessments for ionospheric electron content models. *Journal of Geodesy*, *91*(12), 1405–1414. https://doi.org/10.1007/s00190-017-1032-z

Huang, C. M., Kuo, F. S., Lue, H. Y., & Liu, C. H. (1992). Numerical simulation of the saturated gravity wave spectra in the atmosphere. *Journal of Atmospheric and Solar-Terrestrial Physics*, *54*, 129–142. https://doi.org/10.1016/0021-9169(92)90121-z

Huang, C. S., & Kelley, M. C. (1996a). Nonlinear evolution of equatorial spread F, 1, on the role of plasma instabilities and spatial resonance associated with gravity wave seeding. *Journal of Geophysical Research*, *101*, 283–292. https://doi.org/10.1029/95ja02211

Huang, C. S., & Kelley, M. C. (1996b). Nonlinear evolution of equatorial spread F, 2, Gravity wave seeding of Rayleigh-Taylor instability. *Journal of Geophysical Research*, *101*, 293–302. https://doi.org/10.1029/95ja02210

Huang, C. S., & Kelley, M. C. (1996c). Nonlinear evolution of equatorial spread F, 3, Plasma bubbles generated by structured electric field. *Journal of Geophysical Research*, *101*, 303–313. https://doi.org/10.1029/95ja02209

Huang, X., & Reinisch, B. W. (2001). Vertical electron content from ionograms in real time. *Radio Science*, *36*, 335–342. https://doi.org/10.1029/1999rs002409. https://doi.org/10.1029/1999RS002409

Hysell, D., Larsen, M., Fritts, D., Laughman, B., & Sulzer, M. (2018). Major upwelling and overturning in the mid-latitude F region ionosphere. *Nature Communications*, *9*:3326. https://doi.org/10.1038/s41467-018-05809-x

Hysell, D., Larsen, M., & Sulzer, M. (2016). Observational evidence for new instabilities in the mid-latitude E and F region. *Annals of Geophysics*, *34*, 927–941. https://doi.org/10.5194/angeo-34-927-2016

Jayachandran, B., Krishnankutty, T. N., & Gulyaeva, T. L. (2004). Climatology of ionospheric slab thickness. *Annals of Geophysics*, *22*, 25–33. https://doi.org/10.5194/angeo-22-25-2004

Jin, Y., Spicher, A., Xiong, C., Clausen, L. B. N., Kervalishvili, G., Stolle, C., & Miloch, W. J. (2019). Ionospheric plasma irregularities characterized by the Swarm satellites: Statistics at high latitudes. *Journal of Geophysical Research: Space Physics*, *124*, 1262–1282. https://doi.org/10.1029/2018JA026063

Kelly, M. C., Larsen, M. F., La Hoz, C. A., & McClure, J. P. (1981). Gravity wave initiation of equatorial spread F: A case study. *Journal of Geophysical Research*, *86*, 9087–9100.

Kintner, P. M., Ledvina, B. M., & De Paula, E. R. (2007). GPS and ionospheric scintillations. *Space Weather*, *5*, S09003–n. https://doi.org/10.1029/2006SW000260

Knudsen, D. J., Burchill, J. K., Buchert, S. C., Eriksson, A. I., Gill, R., Wahlund, J.-E., et al. (2017). Thermal ion imagers and Langmuir probes in the Swarm electric field instruments. *Journal of Geophysical Research: Space Physics*, *122*, 2655–2673. https://doi.org/10.1002/2016JA022571

Kuo, F. S., Chou, S. Y., & Shan, S. J. (1998). Comparison of topside and bottomside irregularities in equatorial F region ionosphere. *Journal of Geophysical Research*, *03*(A2), 2193–2199. https://doi.org/10.1029/97ja02586

Kuo, F. S., & Lue, H. Y. (1994). Effect of the wave-shear interaction on gravity wave activity in the lower and middle atmosphere. *Journal of Atmospheric and Terrestrial Physics*, *56*, 1147–1155. https://doi.org/10.1016/0021-9169(94)90053-1

Kuo, F. S., Lue, H. Y., Huang, C. M., Lo, C. L., Liu, C. H., Fukao, S., & Muraoka, Y. (1992). A study of velocity fluctuation spectra in the troposphere and lower stratosphere using MU radar. *Journal of Atmospheric and Terrestrial Physics*, *54*, 31–48. https://doi.org/10.1016/0021-9169(92)90083-w

Li, Z., Yuan, Y., Wang, N., Hernández-Pajares, M., & Huo, X. (2015). SHPTS: Towards a new method for generating precise global ionospheric TEC map based on spherical harmonic and generalized trigonometric series functions. *Journal of Geodesy*, *89*(4), 331–345. https://doi.org/10.1007/s00190-014-0778-9

Liu, J. Y., Chen, C. H., Lin, C. H., Tsai, H. F., Chen, C. H., & Kamogawa, M. (2011). Ionospheric disturbances triggered by the 11 March 2011 M9. 0 Tohoku earthquake. *Journal of Geophysical Research: Space Physics*, *116*(A6), A06319–n. https://doi.org/10.1029/2011JA016761

Liu, L., Le, H., Wan, W., Sulzer, M. P., Lei, J., & Zhang, M. L. (2007). An analysis of the scale heights in the lower topside ionosphere based on the Arecibo incoherent scatter radar measurements. *Journal of Geophysical Research: Space Physics*, *112*, A06307. https://doi.org/10.1029/2007ja012250

Lomidze, L., Knudsen, D. J., Burchill, J., Kouznetsov, A., & Buchert, S. C. (2018). Calibration and validation of Swarm plasma densities and electron temperatures using ground-based radars and satellite radio occultation measurements. *Radio Science*, *53*, 15–36. https://doi.org/10.1002/2017RS006415

Luan, X., Liu, L., Wan, W., Lei, J., Zhang, S.-R., Holt, J. M., & Sulzer, M. P. (2006). A study of the shape of the topside electron density profile derived from incoherent scatter radar measurements over Arecibo and Millstone Hill. *Radio Science*, *41*, RS4006–n. https://doi.org/10.1029/2005RS003367

Makela, J. J., Kelley, M. C., & Beaujardiere, O. (2006). Convective ionospheric storms: A major space weather problem. *Space Weather*, *4*, a–n. https://doi.org/10.1029/2005SW000144

Miller, C. A., Swartz, W. E., Kelley, M. C., Mendillo, M., Nottingham, D., Scali, J., & Reinisch, B. (1997). Electrodynamics of midlatitude spread F, 1. Observations of unstable gravity wave-induced ionospheric electric fields at tropical latitudes. *Journal of Geophysical Research*, *102*, 11521–11532. https://doi.org/10.1029/96ja03839

Nsumei, P., Reinisch, B. W., Huang, X., & Bilitza, D. (2012). New Vary-Chap profile of the topside ionosphere electron density distribution for use with the IRI model and the GIRO real time data. *Radio Science*, *47*, RS0L16. https://doi.org/10.1029/2012rs004989

Olivares-Pulido, G., Hernández-Pajares, M., Aragón-Angel, A., & Garcia-Rigo, A. (2016). A linear scale height Chapman model supported by GNSS occultation measurements. *Journal of Geophysical Research: Space Physics*, *121*, 7932–7940. https://doi.org/10.1002/2016JA022337

Ossakow, S. L. (1981). Spread F theories – A review. *Journal of Atmospheric and Terrestrial Physics*, *43*, 437–452. https://doi.org/10.1016/0021-9169(81)90107-0

Park, J., Kwak, Y.-S., Mun, J.-C., & Min, K.-W. (2015). Vertical scale height of the topside ionosphere around the Korean peninsula: Estimates from ionosondes and the Swarm constellation. *Journal of Astronomy and Space Science*, *32*(4), 311–315. https://doi.org/10.5140/JASS.2015.32.4.311

Perkins, F. (1973). Spread F and ionospheric currents. *Journal of Geophysical Research*, *78*, 218–226. https://doi.org/10.1029/ja078i001p00218

Pignalberi, A., Pezzopane, M., & Rizzi, R. (2018). Modeling the lower part of the topside ionospheric vertical electron density profile over the European region by means of Swarm satellites data and IRI UP method. *Space Weather*, *16*, 304–320. https://doi.org/10.1002/2017SW001790

Reinisch, B. W., & Galkin, I. A. (2011). Global ionospheric radio observatory (GIRO). *Earth Planets and Space*, *63*, 377–381. https://doi.org/10.5047/eps.2011.03.001

Reinisch, B. W., & Huang, X. (2001). Deducing topside profiles and total electron content from bottomside ionograms. *Advances in Space Research*, *27*(1), 23–30. https://doi.org/10.1016/s0273-1177(00)00136-8

Roma-Dollase, D., Hernández-Pajares, M., Krankowski, A., Kotulak, K., Ghoddousi-Fard, R., Yuan, Y., et al. (2018). Consistency of seven different GNSS global ionospheric mapping techniques during one solar cycle. *Journal of Geodesy*, *92*(6), 691–706. https://doi.org/10.1007/s00190-017-1088-9

Saito, A., Nishimura, M., Yamamoto, M., Fukao, S., Kubota, M., Shiokawa, K., et al. (2001). Traveling ionospheric disturbances detected in the FRONT campaign. *Geophysical Research Letters*, *28*, 689–692. https://doi.org/10.1029/2000gl011884

Savastano, G., Komjathy, A., Verkhoglyadova, O., Mazzoni, A., Crespi, M., Wei, Y., & Mannucci, A. J. (2017). Real-time detection of tsunami ionospheric disturbances with a stand-alone GNSS receiver: A preliminary feasibility demonstration. *Science Reports*, *7*, 46607. https://doi.org/10.1038/srep46607

Stankov, S. M., & Jakowski, N. (2006). Topside ionospheric scale height analysis and modeling based on radio occultation measurements. *Journal of Atmospheric and Solar-Terrestrial Physsics*, *68*, 134–162. https://doi.org/10.1016/j.jastp.2005.10.003

Stankov, S. M., Jakowski, N., Heise, S., Muhtarov, P., Kutiev, I., & Warnant, R. (2003). A new method for reconstruction of the vertical electron density distribution in the upper ionosphere and plasmasphere. *Journal of Geophysical Research: Space Physics*, *108*(A5), 1164. https://doi.org/10.1029/2002JA009570

Su, F., Wang, W., Burns, A. G., Yue, X., & Zhu, F. (2015). The correlation between electron temperature and density in the topside ionosphere during 2006–2009. *Journal of Geophysical Research: Space Physics*, *120*, 10724–10739. https://doi.org/10.1002/2015JA021303

Taylor, M. J., Jahn, J. M., Fukao, S., & Saito, A. (1998). Possible evidence of gravity wave coupling into the mid-latitude f region ionosphere during the SEEK campaign. *Geophysical Research Letters*, *25*, 1801–1804. https://doi.org/10.1029/97gl03448

Tsagouri, I., Goncharenko, L., Shim, J. S., Belehaki, A., Buresova, D., & Kuznetsova, M. M. (2018). Assessment of current capabilities in modeling the ionospheric climatology for space weather applications: FoF2 and hmF2. *Space Weather*, *16*, 1930–1945. https://doi.org/10.1029/2018SW002035

Tulasi Ram, S. T., Su, S. Y., Liu, C. H., Reinisch, B. W., & McKinnell, L. A. (2009). Topside ionospheric effective scale heights (HT) derived with ROCSAT-1 and ground-based ionosonde observations at equatorial and midlatitude stations. *Journal of Geophysical Research*, *114*, A10309. https://doi.org/10.1029/2009JA014485

Wang, S., Huang, S., & Fang, H. (2015). Topside ionospheric VARY-chap scale height retrieved from the COSMIC/FORMOSAT-3 data at midlatitudes. *Advances in Space Research*, *56*(5), 893–899. https://doi.org/10.1016/j.asr.2015.04.021

Webb, P. A., Benson, R. F., & Grebowsky, J. (2006). Altitude variations of middle-latitude topside ionospheric electron-density profiles. *Advances in Space Research*, *37*, 951–957. https://doi.org/10.1016/j.asr.2005.05.130

Wielgosz, P., Milanowska, B., Krypiak-Gregorczyk, A., & Jarmoowski, W. (2021). Validation of GNSS-derived global ionosphere maps for different solar activity levels: Case studies for years 2014 and 2018. *GPS Solutions*, *25*:103. https://doi.org/10.1007/s10291-021-01142-x

Woodman, R. F. (1993). Equatorial ionospheric irregularities as observed by the Jicamarca radar. In F.-S. Kuo (Ed.), *Low-latitude ionospheric physics*. *COSPAR Colloq*. Ser. (Vol. 7, pp. 83–95). Elsevier Science.

Woodman, R. F., & La Hoz, C. (1976). Radar observation of F region equatorial irregularities. *Journal of Geophysical Research*, *81*, 5447–5466. https://doi.org/10.1029/ja081i031p05447

Wu, M. J., Guo, P., Chen, Y. L., Fu, N. F., Hu, X. G., & Hong, Z. J. (2020). New Vary-Chap scale height profile retrieved from COSMIC radio occultation data. *Journal of Geophysical Research: Space Physics*, *125*, e2019JA027637. https://doi.org/10.1029/2019JA027637

Yokoyama, T., Hysell, D. L., Otsuka, Y., & Yamamoto, M. (2009). Three-dimensional simulation of the coupled Perkins and Es layer instabilities in the nighttime midlatitude ionosphere. *Journal of Geophysical Research*, *114*, A03308. https://doi.org/10.1029/2008ja013789

Zalesak, S. T., & Ossakow, S. L. (1980). Nonlinear equatorial spread F: Spatially large bubbles resulting from large horizontal scale initial perturbations. *Journal of Geophysical Research*, *85*, 2131–2142. https://doi.org/10.1029/ja085ia05p02131

Zalesak, S. T., Ossakow, S. L., & Chaturvedi, P. K. (1982). Nonlinear equatorial spread F: The effect of neutral winds and background Pedersen conductivity. *Journal of Geophysical Research*, *87*, 151–166. https://doi.org/10.1029/ja087ia01p00151